

# Circumventing Thermodynamic Constraints in Nucleation-Controlled Crystallization of $\text{Al}_2\text{TiO}_5$ -Based Chemical Vapor Deposition Coatings

Sebastian Öhman, Gustav Ek, Gyula Nagy, Tobias Törndahl, Daniel Primetzhofer, and Mats Boman\*



Cite This: <https://doi.org/10.1021/acs.chemmater.2c00615>



Read Online

ACCESS |



Metrics & More



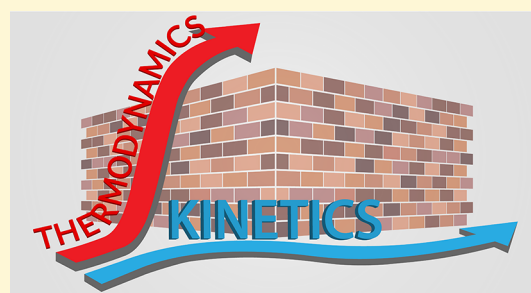
Article Recommendations



Supporting Information

**ABSTRACT:** Nucleation is a fundamental part in most syntheses of ceramic materials. Yet, few techniques enable control of this step, which would offer possibilities to attain full-scale kinetic selectivity of the syntheses to reach novel compounds with unique properties. Herein, we present a nucleation-controlled crystallization pathway to synthesize coatings of aluminum titanate ( $\text{Al}_2\text{TiO}_5$ )—renowned for its low-to-negative thermal expansion—at significantly reduced temperatures than conventional solid-state techniques. Based on a kinetic study using *in situ* X-ray diffraction, detailed mechanistic insights into the crystallization process and phase evolutions within the Al–Ti–O system are obtained. The lowest activation energies for crystallization are given when the Al–Ti ratio is close-to-stoichiometric or Ti-enriched.

Along with these compositions' similar kinetics at the earliest stages of the transformation, a joint nucleation behavior is discovered, revealing the elemental role of titanium in nucleating the main  $\text{Al}_2\text{TiO}_5$  phase. Based on classical nucleation theory, we deduce the significant influence of the configurational entropy ( $S_{\text{config}}$ ) when crystallization occurs in the nucleation-controlled domain. Finally, peculiar transition features are observed in the Al-enriched regime during annealing at intermediate temperatures, whose causes are ascribed to the presence of secondary nucleation events and possibilities of structural relaxations in the amorphous matrixes when crystallizing.



## INTRODUCTION

Developing novel materials with improved properties hinges on finding more efficient and adaptive ways to make them. In the syntheses of many inorganic materials, the reactions involved are typically limited by diffusion,<sup>1–4</sup> owing to energetically stable reactants and low thermodynamically driving forces to yield the desired products.<sup>5,6</sup> To mitigate these issues, elevated temperatures and prolonged reaction times are frequently used to enhance the otherwise slow mass transfer rates,<sup>7,8</sup> strategies that have traditionally been<sup>9,10</sup>—and still remain<sup>11</sup>—conventional routes for accessing many ceramics materials.<sup>6</sup> However, these approaches are insufficient in pursuing novel multicomponent phases, carrying potentially improved properties, as they tend to favor the most thermodynamically stable ones and those having the simplest (binary) stoichiometries.<sup>1,12</sup> Moreover, although most of the thermodynamic space of binary compounds has already been explored or predicted, a vast and partially uncharted dimension beyond these exists in the domain of metastability.<sup>12,13</sup> Besides the necessities of thermodynamic control,<sup>7,12</sup> the capability to isolate and discover such phases requires an additional component not readily offered in many solid-state methods;<sup>14</sup> namely, the kinetic selectivity of the synthesis.<sup>5,15</sup> Syntheses incorporating this selectivity have the potential to circumvent common thermodynamic constraints and enable kinetical

routes to form compounds at reduced temperatures, shorter timescales, and with higher phase purities.<sup>6,16</sup> These approaches also carry the prospective to encapsulate the computational prediction,<sup>11</sup> rational planning,<sup>1,17</sup> and selective design<sup>9</sup> of novel compounds into a common synthesis framework, a cornerstone that—unlike organic chemistry<sup>10,16</sup>—is still lagging in the field of inorganic chemistry.<sup>7,18</sup> Although many alternative synthesis routes have been developed,<sup>15,18,19</sup> few provide opportunities to adjust the reaction coordinates and attain predictable phase selectivity by coherent modifications of the involved reactants.<sup>1,17</sup> Fewer allow controlling the most initial and fundamental parts of any phase evolution, which is typically ruled by nucleation, rather than diffusion.<sup>11,20</sup>

Nonetheless, in the early nineties, Novet *et al.* demonstrated a new approach to reach the domain of extended solids, using thin amorphous layers as reaction intermediates.<sup>5</sup> Following the pioneering explorations of reaction kinetics in the 1970s

Received: February 25, 2022

Revised: May 4, 2022

and 1980s,<sup>21–29</sup> Novet *et al.* illustrated how the stabilization and subsequent crystallization of these layers yielded reaction pathways that were controlled by nucleation, not diffusion. Their synthesis route allowed them to bypass diffusion as the rate-limiting step, forming ternary compounds without developing binary ones, and the capability to predict and control what phases were to be made in their studied Fe–Si system. Novet *et al.*'s work was a breakthrough in developing many synthetic and soft chemistry-based techniques seen in modern application areas. Since then, their work has also been followed by several other groups.<sup>1,2,4,6,15,16,30</sup>

Recently, we have shown a comparable synthesis route to prepare amorphous coatings by the simultaneous depositions of alkoxide-based precursors using an in-house-developed chemical vapor deposition (CVD) process.<sup>31</sup> Specifically, we have demonstrated how amorphous layers of aluminum titanate ( $\text{Al}_2\text{TiO}_5$ )—renowned for displaying a low-to-negative thermal expansion,<sup>32,33</sup> good corrosion resistance,<sup>34,35</sup> and self-healing capabilities<sup>36,37</sup>—can be synthesized at much lower temperatures and shorter timescales than comparable solid-state techniques. Upon annealing, our coatings undergo an amorphous-to-crystalline transition without yielding significant amounts of binary constituents, like  $\text{Al}_2\text{O}_3$  and  $\text{TiO}_2$ , which are commonly found as residues from the solid-state route.

In addition, our developed method provides evidence of new phenomena in the Al–Ti–O system. First, by altering the concentrations of the reactants, we can tailor the composition and corresponding Al–Ti ratio of the amorphous coatings, even though  $\text{Al}_2\text{TiO}_5$  is represented as a single-line phase in the conventional  $\text{Al}_2\text{O}_3$ – $\text{TiO}_2$  pseudo-binary phase diagram.<sup>38–41</sup> Second, our deposition method operates well below the typical formation temperatures to obtain the  $\text{Al}_2\text{TiO}_5$  phase (*i.e.*, above 1300 °C) and in a temperature regime where the solid-state route predicts the phase's thermal decomposition, rather than its formation.<sup>42,43</sup> Third, besides the main  $\text{Al}_2\text{TiO}_5$  phase, our explorations in the Al–Ti–O system led us to discover unconventional and structurally related phases, like  $\text{Al}_6\text{Ti}_2\text{O}_{13}$  and  $\text{Al}_{16}\text{Ti}_5\text{O}_{34}$ , whose existences have earlier been proposed by authors in the field.<sup>38,41,44,45</sup> However, the mechanisms and reaction conditions governing these phases' formations and crystallization behaviors are still unknown, likewise the possibilities of adapting the main  $\text{Al}_2\text{TiO}_5$  phase by the said synthesis route.

Therefore, in this study, we present a multivariate kinetic study, wherein the compositional and temperature space governing the crystallization of these phases is thoroughly investigated. By utilizing *in situ* heating X-ray diffraction (XRD), we obtain mechanistic insights into the phase evolutions of the amorphous coatings with various Al–Ti stoichiometries. Principally, information concerning the overall crystallization rate,  $K$ , and dimensionality of the crystallization process,  $n$ , is derived by using the Johnson<sup>46</sup>–Mehl<sup>47</sup>–Avrami<sup>48–50</sup>–Kolmogorov<sup>51</sup> (JMAK) equation, which is expressed as

$$V_t = 1 - \exp(-Kt^n) \quad (1)$$

where  $V_t$  is the crystallized volume fraction and  $t$  is the time required to reach a given volume fraction. From Arrhenius relationships, we attain apparent activation energies representative of the entire crystallization process. Our main findings emphasize the role of nucleation during crystallization. We also reveal the elemental involvement of titanium and highlight the significant contribution of the configurational entropy to the

displayed crystallization behaviors. Finally, peculiar transition features are encountered in the Al-enriched regime, whose causes are linked to our previous Raman spectroscopic findings, showing that structural relaxations can occur in the amorphous coatings during annealing.<sup>31</sup> Accordingly, the expositions made in this study build on our previous synthetic investigations and help understand the role of nucleation and growth in the synthesis and phase selections within the Al–Ti–O system.

## METHODOLOGY

Amorphous  $\text{Al}_2\text{TiO}_5$ -based coatings with various Al–Ti ratios were deposited using an in-house-developed CVD reactor, whose instrumental details are presented elsewhere.<sup>31</sup> Depositions were carried out from simultaneous use of two metal–organic alkoxide precursors, aluminum isopropoxide (AIP) and titanium isopropoxide (TIP), at 450 °C for 1 h on Si P-type (100) substrates. The Al–Ti ratio in the coatings was controlled by altering the heating temperature (and corresponding vapor pressure) of the more volatile TIP precursor. Detailed experimental descriptions of the deposition process can be found in ref 31. The compositions were cross-evaluated for their Al–Ti ratios using energy-dispersive spectrometry (EDS) and Rutherford backscattering spectrometry (RBS). Four different Al–Ti batch compositions were synthesized, corresponding to Al-enriched, ~ideal (2:1), equimolar (1:1), and Ti-enriched, whose evaluated stoichiometries are summarized in Table 1.

**Table 1. Al–Ti Ratios Corresponding to the Four Evaluated Compositions Al-Enriched, ~Ideal, Equimolar (1:1), and Ti-Enriched**

| method | Al-enriched | ~ideal | 1:1  | Ti-enriched |
|--------|-------------|--------|------|-------------|
| EDS    | 2.86        | 1.94   | 1.10 | 0.44        |
| RBS    | 2.87        | 1.93   | 1.00 | 0.54        |

In order to follow the dynamics of crystallization, *in situ* heating XRD experiments were carried out in the  $2\theta$  range 32.5–36° using a monochromatized Cu  $K\alpha$  radiation source (40 kV and 40 mA) in a D8 ADVANCE diffractometer (Bruker). The narrow  $2\theta$  interval was chosen to maximize the intensity output and time resolution of the most substantial Bragg peaks appearing in the diffractogram. Additional *ex situ* XRD measurements of the annealed samples using longer scan ranges can be found in the Supporting Information, Figure S18. The *in situ* instrument was equipped with a Lynx-eye XE position-sensitive detector and a radial heater furnace cell (Anton Paar) fitted with a thermocouple unit close to the heated sample. All experiments were carried out in a Bragg–Brentano configuration and a helium atmosphere to exclude possible effects from the surrounding air environment. Measurements were made by ramping up the temperature from room temperature to different isothermal annealing temperatures, using a heating rate of 6 °C/min and a step size of 0.06°. The progress of crystallization was continuously monitored by repeated  $\theta/2\theta$  scans, where each scan took about 20 min to complete. The data were then analyzed by fitting a few (1–3) selected Bragg reflections, described in Table 2, using software Topas 6 Academic running in a sequential mode.<sup>52</sup> All peaks were modeled using a Thompson–Cox–Hastings' pseudo-Voigt function and the background with a

**Table 2. List of Analyzed Bragg Reflections and Their Corresponding Data Values**

| phase  | 2 $\theta$ | d-value (Å) | hkl    | refs |
|--|------------|-------------|--------|------|
| Al <sub>2</sub> TiO <sub>5</sub>                 | 33.721     | 2.65578     | (023)  | 42   |
| Al <sub>6</sub> Ti <sub>2</sub> O <sub>13</sub>  | 34.367     | 2.60731     | (024)  | 45   |
| Al <sub>16</sub> Ti <sub>5</sub> O <sub>34</sub> | 34.654     | 2.58633     | (0221) | 38   |

sixth-order Chebyshev polynomial. In a typical refinement, only the peak positions and areas were refined.

Assuming that the adsorption coefficient is negligible in the coatings—which usually is the case among thin films and coatings<sup>29</sup>—and that no significant change in texturing occurs throughout the phase transformation,<sup>53</sup> the diffracted Bragg intensity  $I$  can, at any given time  $t$ , be treated according to<sup>53,54</sup>

$$\begin{cases} I(t) \propto V_t & \text{(I)} \\ 0 \leq V_t \leq 1 & \text{(II)} \\ I_t^{\text{norm}} \equiv V_t^{\text{norm}} & \text{(III)} \end{cases} \quad (2)$$

where  $V_t$  denotes the volume fraction transformed of the crystalline phase in the analyzed sample. Because  $V_t$  is enclosed in  $[0, 1]$ , unity-based normalization of the obtained intensity data must be made from the equation<sup>53</sup>

$$I_t^{\text{norm}} = \frac{I_t - I_0}{I_\infty - I_0} \quad (3)$$

where  $I_t^{\text{norm}}$  is the total gross counts at  $t$ ,  $I_0$  is the background intensity, and  $I_\infty$  is the constant gross counts at the end of the run period. By convention,  $I_\infty$  is defined as the  $I_{0.99}$  level, that is, where 99% of the crystallization has been completed. To track the kinetics of transformation,  $V_t$  is plotted against  $t$ , which typically displays a sigmoidal-shaped curve following the JMAK equation (eq 1). The two kinetic parameters  $K$  and  $n$  can then be obtained from the equation by rewriting it into a double-logarithmic function

$$\ln(-\ln(1 - V_t)) = \ln K + n \ln t \quad (4)$$

which allows  $\ln K$  and  $n$  to be determined from linear regression analysis by plotting  $\ln\left(\ln \frac{1}{1 - V_t}\right)$  versus  $\ln t$  within the isokinetic regime, where nucleation and growth are regarded as time-invariant parameters.<sup>48,49,55</sup>

Although  $K$  is a constant related to the overall crystallization rate, it is essential to note that it is not a “true” rate constant in the strictest sense because it simultaneously incorporates the rates from nucleation and growth.<sup>56</sup> In other words,  $K$  does not truly represent any proper elementary step under the first-order mechanism of crystallization,<sup>56</sup> which the JMAK

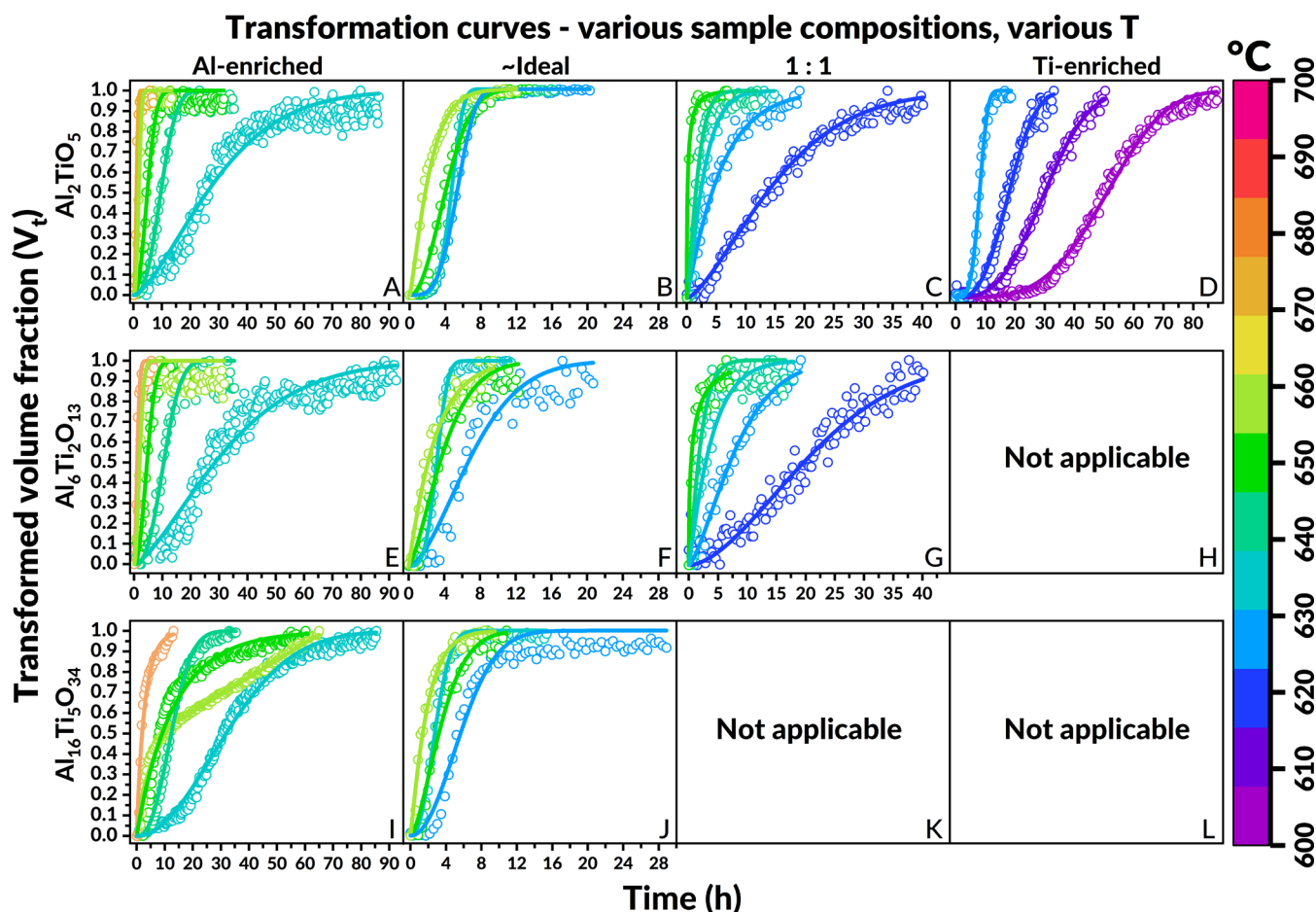


**Figure 1.** Transformation curves illustrating the influence of variations in isothermal annealing temperatures and changes in chemical composition (Al–Ti ratios) of the amorphous matrixes. Each horizontal row represents the crystallization of the Al<sub>2</sub>TiO<sub>5</sub>, Al<sub>6</sub>Ti<sub>2</sub>O<sub>13</sub>, and Al<sub>16</sub>Ti<sub>5</sub>O<sub>34</sub> phases. “Not applicable” means that any emerging peak assignable to Al<sub>6</sub>Ti<sub>2</sub>O<sub>13</sub> or Al<sub>16</sub>Ti<sub>5</sub>O<sub>34</sub> has too low intensity development to allow extraction of kinetic data in this region.



equation and classical nucleation theory regularly assume.<sup>53,56</sup> Indeed, in most crystallization processes, nucleation will proceed so fast compared to the growth stage that the entire process may practically be regarded as a (pseudo)-first-order transformation limited primarily to diffusion.<sup>54,57</sup> However, during circumstances where the role of nucleation becomes significant or even rate-determining, the lack of a saturated nucleation rate, especially at the earliest stages of crystallization, may strongly affect the physical meaning of  $K$ .<sup>53</sup> Therefore, one should be careful of using  $K$  as a parameter in any further interpretation of, for example, activation energies.

Instead, an expression for the apparent activation energy representative of the entire crystallization process,  $E_a^{\text{app}}$ , can be derived by noting that the time  $t_x$  required to reach a certain crystalline volume fraction, for example,  $t_{0.05}$ ,  $t_{0.50}$ , and  $t_{0.99}$ , frequently follows an Arrhenius-like relationship<sup>58–62</sup>

$$t_x = t_0 \cdot \exp \frac{E_a^{\text{app}}}{RT} \quad (5)$$

where  $t_0$  is a pre-exponential constant,  $R$  is the universal gas constant, and  $T$  is the temperature given in Kelvin. Hence, a plot of  $\ln t_x$  versus  $1/T$  typically gives a straight line whose slope relates to the apparent activation energy given at specific volume fractions. At the beginning of the transformation,  $t_x$  is governed by nucleation, so that  $E_a^{\text{app}}$  predominantly relates to the barrier of nucleation.<sup>58,63</sup> Similarly, during the last stages of transformation, where nucleation typically has ceased,  $E_a^{\text{app}}$  links more with the energetic barrier of growth.<sup>57</sup> Accordingly, this treatment of the apparent activation energy<sup>63</sup> allows a formalized decoupling of the two energetic contributions of nucleation and growth during the initial and final stages of crystallization.

## RESULTS

**Effect of Temperature.** Figure 1 shows transformation curves for various sample compositions and temperatures. A strong temperature dependency on the transition rates is evident in all graphs, indicating that an incremental increase in isothermal heating yields drastically shorter times needed to reach the final crystalline product. The effect is most pronounced in cases where the composition deviates from the ~ideal stoichiometry and is particularly noticeable in the domain with increased titanium content (*i.e.*, 1:1 and Ti-enriched). Notably, the strong temperature dependency on the transformation rates is a signifying feature of a nucleation-controlled crystallization process.<sup>20</sup>

Figure 2 illustrates contour maps of the relative phase fractions for  $\text{Al}_2\text{TiO}_5$ ,  $\text{Al}_6\text{Ti}_2\text{O}_{13}$ , and  $\text{Al}_{16}\text{Ti}_5\text{O}_{34}$  as a function of variable temperature and sample composition. The relative phase fractions are derived by comparing each phase's area intensity at the end of every annealing period. In the equimolar 1:1 and Ti-enriched domains, besides the three phases mentioned above,  $\text{TiO}_2$  (anatase) readily forms as well, which agrees with our previous studies.<sup>31</sup> Detailed phase formation analyses depending on the samples' Al–Ti ratios can also be found in this study's [Supporting Information](#), Figure S18.

Regarding the annealing temperatures, there is no obvious impact on the preferential formation of either  $\text{Al}_2\text{TiO}_5$ ,  $\text{Al}_6\text{Ti}_2\text{O}_{13}$ , or  $\text{Al}_{16}\text{Ti}_5\text{O}_{34}$ . This is accentuated by the almost vertical contour lines seen in Figure 2. In contrast, a clear

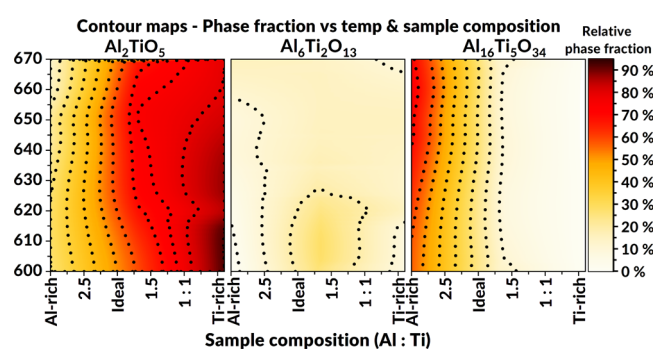


**Figure 2.** Contour maps showing the relative phase fractions (colored) of the three phases  $\text{Al}_2\text{TiO}_5$ ,  $\text{Al}_6\text{Ti}_2\text{O}_{13}$ , and  $\text{Al}_{16}\text{Ti}_5\text{O}_{34}$  with variable isothermal annealing temperature and composition (Al–Ti ratio).

influence of the sample composition (Al–Ti ratio) is evident, which is further described in the following section.

**Effect of Composition.** Analogous to the effect of temperature, the composition of the amorphous (as-deposited) samples significantly influences the observed transformation rates. As seen in Figure 1, the crystallization is more sluggish and takes longer times to complete in the Al-enriched domain, particularly for intermediate and late transformation stages. Additionally, transformations require higher temperatures to both commence and finish when the aluminum content increases, which shows a higher transformation resilience and a more considerable thermal stability of the amorphous matrixes in this compositional domain. Interestingly, the ~ideal sample did not display the lowest achieved crystallization temperatures. Instead, the crystallization temperatures continuously decrease when the titanium content increases (and the Al–Ti ratio decreases). In other words, there is a constant trend in the lowest achieved crystallization temperature from Al-enriched to Ti-enriched, suggesting that nucleation happens more preferentially when the titanium content increases.

Contrary to the other compositions, the existence of the  $\text{Al}_{16}\text{Ti}_5\text{O}_{34}$  phase is more extensive when the Al-enriched regime is reached. Also, although the  $\text{Al}_6\text{Ti}_2\text{O}_{13}$  phase appears even when the stoichiometry becomes equimolar or Ti-enriched,  $\text{Al}_{16}\text{Ti}_5\text{O}_{34}$  does not readily develop when the titanium content increases. Therefore, higher aluminum content in the amorphous matrixes seems to correlate with the formation of the  $\text{Al}_{16}\text{Ti}_5\text{O}_{34}$  phase, which conforms to earlier examinations made by Hoffmann *et al.*<sup>38</sup> Besides the transformation curves seen in Figure 1, this notion is also expressed by the contour maps in Figure 2, where a sharp increase in relative phase fractions for  $\text{Al}_{16}\text{Ti}_5\text{O}_{34}$  occurs when the Al-enriched domain is reached.

Noticeable in the Al-enriched domain, a peculiar growth behavior appears for the  $\text{Al}_{16}\text{Ti}_5\text{O}_{34}$  phase when intermediate annealing temperatures (660 °C) are used. As seen in Figure 1(I), the transformation curve initially follows a comparable progression to the other examined compositions. However, after completing around 40% of the volume fraction, the slope of the transformation curve declines markedly and reaches a linear region that does not cease its transformation even after a prolonged annealing duration (65 h). This behavior deviates from the conventional sigmoidal-shaped transformation curves observed for the other annealing temperatures. Moreover, it occurs only for the  $\text{Al}_{16}\text{Ti}_5\text{O}_{34}$  phase when the amorphous sample is Al-enriched.

To explore the possible causes of this behavior, a plot of measured  $2\theta$ -values versus time was made based on the XRD data. As seen in Figure 3, the  $2\theta$ -values continuously shift to lower values for the  $\text{Al}_{16}\text{Ti}_5\text{O}_{34}$  phase as the crystallization progresses. Meanwhile, the same values increase for the  $\text{Al}_6\text{Ti}_2\text{O}_{13}$  phase, whereas no apparent change occurs for the  $\text{Al}_2\text{TiO}_5$  phase. Hence, this indicates a continuous increase in unit cell parameters for the  $\text{Al}_{16}\text{Ti}_5\text{O}_{34}$  phase while the same values for the  $\text{Al}_6\text{Ti}_2\text{O}_{13}$  phase concurrently diminish. Consequently, these combined observations suggest that an intertwined relationship between the  $\text{Al}_6\text{Ti}_2\text{O}_{13}$  and  $\text{Al}_{16}\text{Ti}_5\text{O}_{34}$  phases exist. Also, Figure 3 indicates that  $\text{Al}_{16}\text{Ti}_5\text{O}_{34}$  is forming at the expense of  $\text{Al}_6\text{Ti}_2\text{O}_{13}$ .

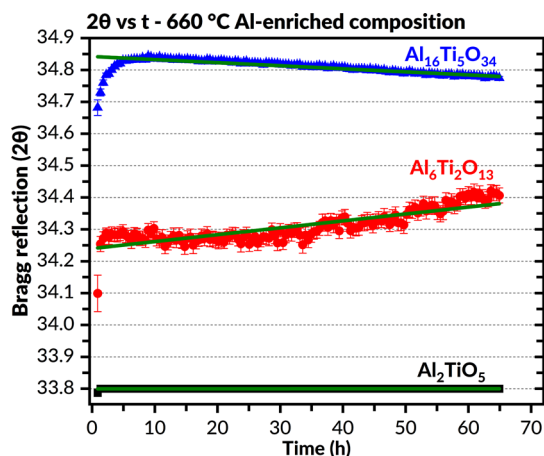


**Figure 3.**  $2\theta$  vs time plot illustrating a continuous shift in  $2\theta$ -values between  $\text{Al}_{16}\text{Ti}_5\text{O}_{34}$  and  $\text{Al}_6\text{Ti}_2\text{O}_{13}$  for Al-enriched samples annealed at 660 °C. The green line marks trends in data progression.

**Kinetic Parameters.** Figure 4 compiles the derived kinetic parameters ( $\ln K$  and  $n$ ) based on the JMAK equation for various Al–Ti ratios. Additional derivation of the parameters by so-called “Avrami plots” (also known as “Sharp–Hancock” plots) can be found in the Supporting Information Figures S13–S16. On immediate inspection of Figure 4, an inverse correlation between  $\ln K$  and  $n$  is discovered. When the kinetic parameter  $n$  diminishes, the corresponding value of  $\ln K$  increases (and *vice versa*). Accordingly, a lower dimensionality in the crystallization behavior relates to a higher transformation rate and a more heterogenous, confined character of the transformation. Similar to the transformation rates, the value of  $n$  changes strongly with both the annealing temperature and the sample composition. In addition,  $n$  may also possibly change with the progress of crystallization, as implied by the behavior seen in the Al-enriched domain. Generally, the dimensionality of crystallization ( $n$ ) reaches its highest value at low isothermal annealing temperatures, whereupon it decreases as the annealing temperature successively increases. This is especially noticeable for the  $\sim$ ideal and equimolar 1:1 stoichiometry. In terms of the  $\sim$ ideal case, the value of  $n$  is the highest for the lowest annealing temperatures (around 4.5 for  $\text{Al}_2\text{TiO}_5$ ) and remains relatively constant until about 645 °C, where a sudden drop in  $n$ —and a corresponding increase in  $\ln K$ —happens. The Al-enriched case demonstrates slightly lower  $n$  values on average, but unlike the  $\sim$ ideal case, there is no similar sharp decline in the  $n$  value when the annealing temperatures increases.

When Al-enriched samples were annealed at intermediate temperatures, two linear regions with markedly different slopes were found in the Avrami plot. This behavior corresponds to the transformation behavior seen in Figure 1(I). The derived kinetic parameters representing the first initial zone, marking a transition up to approximately 40% volume fraction, appear to occur at much slower rates (lower  $\ln K$ ) and with less dimensional constraints (higher  $n$ ) than the subsequent process. In other words, the second regime marks a more confined and faster transition process than the previous, initial one. Therefore, different kinetic parameters before and after 40% volume fraction are obtained, indicating that the transformation behavior changes during the crystallization. In the discussion, we describe the origin of the second regime to occurrences of secondary nucleation, which are triggered by structural relaxations of the amorphous matrixes during their crystallization.

The large values of  $n$ , seen particularly at lower annealing temperatures, support an unconstrained three-dimensional (isotropic) nucleation happening homogeneously in the amorphous matrix.<sup>64</sup> Typically,  $n$  may adopt values between 1 and 4,<sup>65</sup> and values outside this range are frequently considered anomalous. Nevertheless, both higher and lower values of  $n$  have been reported during the crystallization of many amorphous materials,<sup>66–68</sup> including those of metallic glasses.<sup>64,69</sup> For example, large values of  $n$  signify the presence of a transient (time-dependent) and nucleation-assisted crystallization process.<sup>64,65,68,70</sup> In this regard, the  $\sim$ ideal and Ti-enriched samples exhibit the largest values of  $n$  during their crystallization, especially at the lowest annealing temperatures. Although no clear trend in  $n$  could be observed for the Ti-enriched case, its values remained large, regardless of the used annealing temperatures. Contrariwise, the lowest values of  $n$  are found in the 1:1 domain, whose samples also generally displayed the highest  $\ln K$  values, particularly when the annealing temperature was increased.

**T–T–T-Diagrams.** Time–temperature–transformation (T–T–T) diagrams were made based on the transformation curves in Figure 1, which can be found in Figure 5. The three border lines in each window represent the time required to reach 5, 50, and 99% transformed volume fractions for each sample composition and phase. The figure reveals that the formation of  $\text{Al}_2\text{TiO}_5$ ,  $\text{Al}_6\text{Ti}_2\text{O}_{13}$ , and  $\text{Al}_{16}\text{Ti}_5\text{O}_{34}$  is highly intertwined and there is no distinct separation between them.

The T–T–T diagrams detail the strong temperature dependencies seen during the crystallization. In particular, a significant temperature dependency on the initial 5% transformation line is evident for all examined transformations. A similar trend for the 50% transformation line is also observed for the  $\sim$ ideal composition, suggesting a swift transition once nucleation has started. In contrast, the time required to reach the 99% level remained almost vertical for the  $\sim$ ideal composition, implying that the mechanisms controlling the later stages of transformation are virtually unaffected by the increase in annealing temperature. Similar behaviors can also be observed among the equimolar and Ti-enriched compositions. Consequently, the strong temperature dependency of the crystallization, initially seen in Figure 1 and further accentuated in Figure 5, can thus be traced to events happening at the earliest stages of the transformation, that is, to events relating more to nucleation, rather than growth by diffusion.

**Activation Energies.** Figure 6 demonstrates the calculated apparent activation energies ( $E_a^{\text{app}}$ ) for the crystallization of

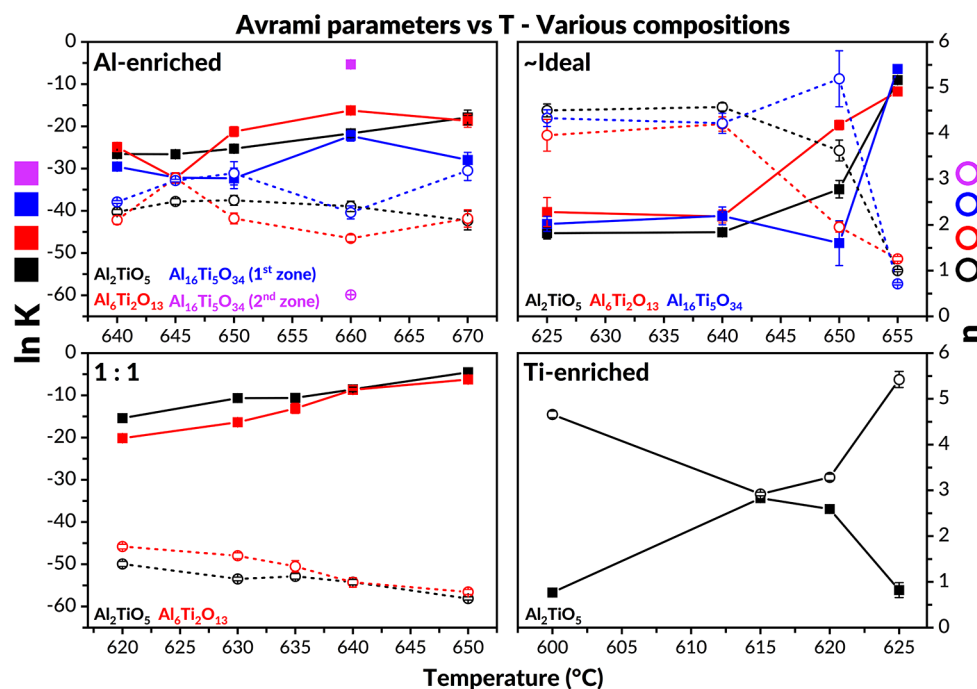


**Figure 4.** Derived kinetic parameters ( $\ln K$  and  $n$ ) for various Al–Ti ratios. Black, red, and blue lines denote values belonging to the  $\text{Al}_2\text{TiO}_5$ ,  $\text{Al}_6\text{Ti}_2\text{O}_{13}$ , and  $\text{Al}_{16}\text{Ti}_5\text{O}_{34}$  phases, respectively. The purple color illustrates kinetic parameters derived from the secondary regime when Al-enriched samples are annealed at 660 °C. Values of  $\ln K$  are expressed with a boxed (■) symbol and  $n$  is expressed with a circular (○) ditto. Certain error bars are found in the plot symbols. For derivations of kinetic parameters from the corresponding Avrami plots, the reader is referred to the [Supporting Information](#).

$\text{Al}_2\text{TiO}_5$ ,  $\text{Al}_6\text{Ti}_2\text{O}_{13}$ , and  $\text{Al}_{16}\text{Ti}_5\text{O}_{34}$  at various sample compositions. As seen in this figure, there are significant differences in calculated  $E_a^{\text{app}}$  values depending on the samples' Al–Ti ratios. For instance, the Al-enriched and equimolar 1:1 sample environments consistently demonstrated the highest  $E_a^{\text{app}}$  values throughout their transformations. With exemption from the  $\text{Al}_6\text{Ti}_2\text{O}_{13}$  phase, the  $E_a^{\text{app}}$  values did not vary markedly in the Al-enriched environment either and remained relatively large throughout the crystallization. In comparison, the activation energies for the 1:1 composition diminished slowly but consistently to lower values as the transition (and crystallized volume fraction) progressed. A similar lowering of apparent activation energies with increasing crystallized volume fraction is also observed for the ~ideal case, which demonstrated the lowest  $E_a^{\text{app}}$  values for its transformation. The lowest value,  $112 \pm 9 \text{ kJ mol}^{-1}$ , is reached after about 75% volume fraction has been completed. For comparison, this value is less than half the magnitude of typical  $E_a^{\text{app}}$  values relating to diffusion in amorphous alloys.<sup>59</sup>

The ~ideal composition displayed an increased uncertainty in determining apparent activation energies at the earliest stages of crystallization. Expressed by the Arrhenius plots found in the [Supporting Information](#) (Figure S17), this uncertainty can be traced to the non-Arrhenius-like behavior and reduced linearity of the regression analysis at the 5% level. Typically, such a behavior can be associated with a time-dependent nucleation rate,<sup>71</sup> a temperature-dependent activation energy,<sup>72</sup> or both. In either case, such a behavior marks a crystallization process primarily driven by nucleation,<sup>71</sup> a theme that is further expounded in the discussion section.

An increased level of uncertainty in determining the apparent activation energies is also noticeable for the Al-enriched case at its late transition stages. Particularly, this is the

case if the 660 °C transition is included when calculating the apparent activation energies of crystallization for  $\text{Al}_{16}\text{Ti}_5\text{O}_{34}$ . This scenario is represented by the gray extension line found in [Figure 6](#). However, such interpretation confounds the otherwise reasonable linear slope of the Arrhenius plot as the duration required to reach the 75 and 99% transformed levels then takes exceedingly long to make. Alternatively, if the transition seen at 660 °C is treated as a separate and subsequent event, hence excluding it from the primary process' data set, an improved linearity and reduced statistical error from the Arrhenius plot is obtained. This outcome is represented by the blue line in [Figure 6](#). Accordingly, this treatment of outlying values signifies that several possible mechanisms may be involved in forming the  $\text{Al}_{16}\text{Ti}_5\text{O}_{34}$  phase, especially when the amorphous stoichiometry is Al-enriched. These mechanisms include possibilities of secondary nucleation and Ostwald ripening, which we explain in the second part of the discussion section.

Concerning the Ti-enriched regime, relatively constant and low  $E_a^{\text{app}}$  values are obtained during crystallization. The average  $E_a^{\text{app}}$  value, representative of the  $\text{Al}_2\text{TiO}_5$  phase, was calculated to be  $425 \pm 75 \text{ kJ mol}^{-1}$ . To better compare this value with the other compositions and phases, a bar diagram was constructed, which can be viewed in [Figure 7](#). In essence, the chart emphasizes that the lowest  $E_a^{\text{app}}$  values are obtained when the stoichiometry is either ~ideal or Ti-enriched.

## DISCUSSION

**Nucleation-Controlled Crystallization.** The present study illustrates how nucleation has a decisive role in crystallizing  $\text{Al}_2\text{TiO}_5$  and its co-forming phases at low temperatures. Principally, this is realized from viewing the combined results concerning the ~ideal stoichiometry. Not

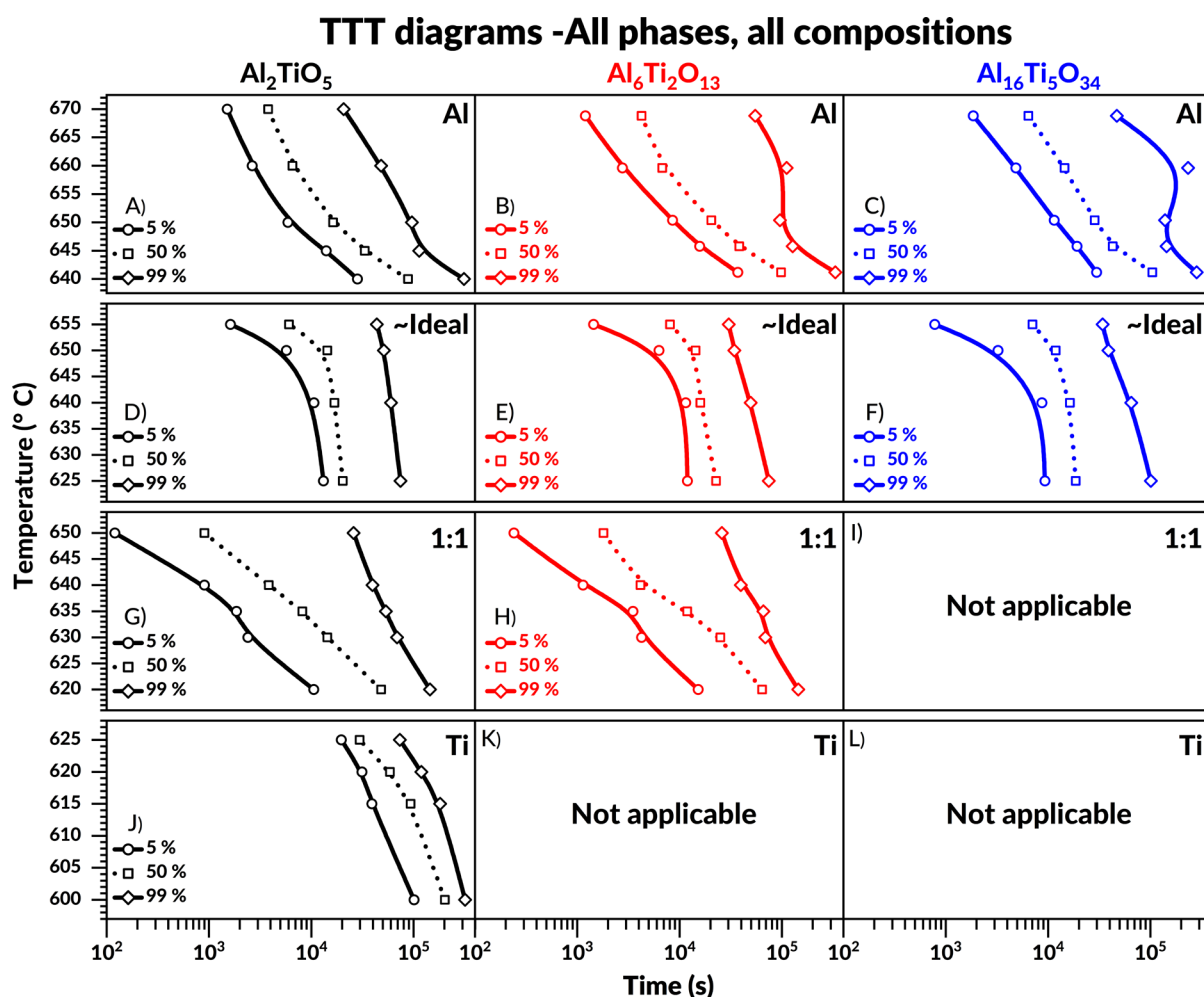


**Figure 5.** T–T–T diagrams showing the formation of  $\text{Al}_2\text{TiO}_5$  (black),  $\text{Al}_6\text{Ti}_2\text{O}_{13}$  (red), and  $\text{Al}_{16}\text{Ti}_5\text{O}_{34}$  (blue) for various Al–Ti stoichiometries. “Not applicable” means that any emerging peak assignable to  $\text{Al}_6\text{Ti}_2\text{O}_{13}$  or  $\text{Al}_{16}\text{Ti}_5\text{O}_{34}$  has too low intensity development to allow any extraction of kinetic data in this region.

only did the  $\sim$ ideal stoichiometry demonstrate a strong temperature dependency on its initial transformation rates but also among the largest Avrami parameter  $n$  and lowest average  $E_a^{\text{app}}$  values during crystallization. Moreover, all compositions generally displayed their largest  $E_a^{\text{app}}$  values at the earliest crystallization stages, indicating that nucleation is the rate-determining event.<sup>1,73</sup> These combined observations support a nucleation-controlled crystallization process,<sup>1,20,74</sup> whose implications are discussed in this section.

According to classical nucleation theory, nucleation control can mainly be achieved by increasing the supersaturation, supercooling, or doing both simultaneously.<sup>20,74,75</sup> The effect of varying the supersaturation (expressed from the variable Al–Ti ratios) and the supercooling (annealing temperature) are both reflected in this study’s results. First, in terms of supercooling, all samples crystallized below half the melting points of their corresponding crystalline states. At such low temperatures, the level of supercooling is extensive; therefore, the total driving force for nucleation ( $\Delta G_n$ ) becomes the dominating parameter influencing the entire crystallization process from a thermodynamic point of view.<sup>59,76,77</sup> This can be accentuated from an expression of the steady-state nucleation rate  $I_{\text{st}}$ , which follows<sup>76,78</sup>

$$I_{\text{st}} = I_0 \cdot \exp\left(-\frac{W^* + \Delta G_D}{k_B T}\right) \quad (6)$$

where  $I_0$  is a pre-exponential factor,  $k_B$  is Boltzmann’s constant, and  $T$  is the annealing temperature. Also,  $W^*$  represents the energetic barrier of nucleation, whereas  $\Delta G_D$  represents the kinetic ditto. By assuming the formation of a spherical nucleus having a critical radius  $r^*$ ,  $W^*$  can be written into<sup>76,78,79</sup>

$$W^* = \frac{16\pi\gamma^3}{3\Delta G_n^2} \quad (7)$$

where  $\gamma$  denotes the crystal amorphous interfacial energy. In this equation,  $\Delta G_n$  represents the sum of all Gibbs free energy changes involved during nucleation. In the cases of amorphous thin films and coatings, the three main contributions to  $\Delta G_n$  can arithmetically be combined according to the following equation

$$\Delta G_n = \Delta G_v + \Delta G_s + \Delta G_e \quad (8)$$

where  $\Delta G_v$  is the volume free energy of the crystalline phase,  $\Delta G_s$  the surface free energy, and  $\Delta G_e$  denotes the strain energy caused mainly by variations in densities between the amorphous and crystalline states.<sup>80</sup> The latter term may also



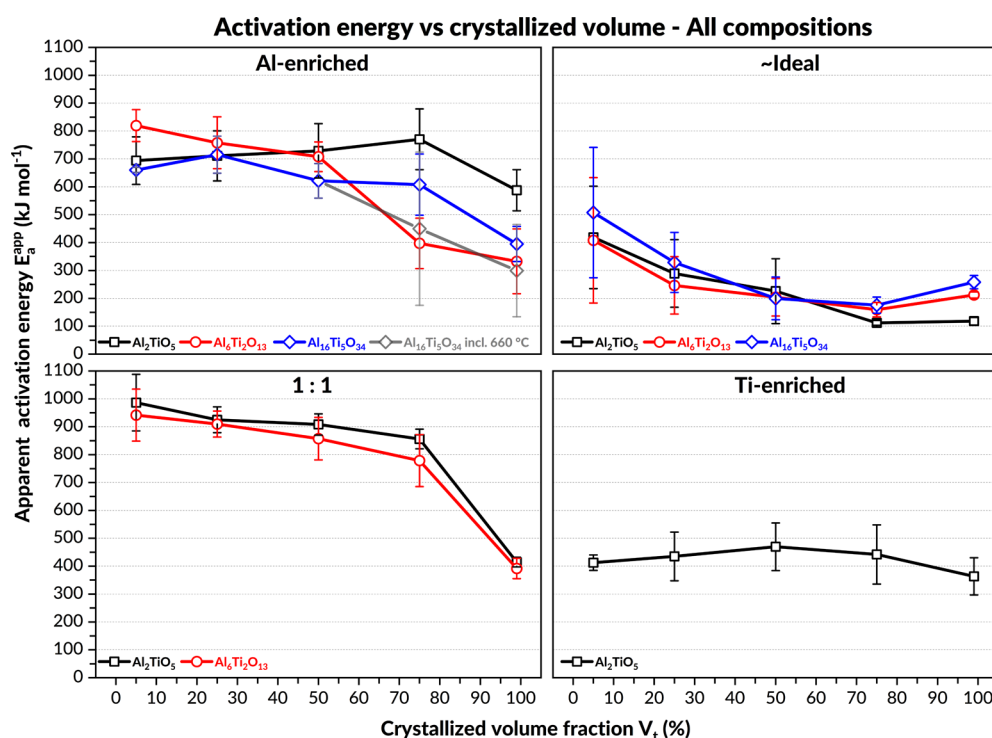


Figure 6. Apparent activation energies ( $E_a^{\text{app}}$ ) derived at different transformation stages and various Al–Ti ratios.

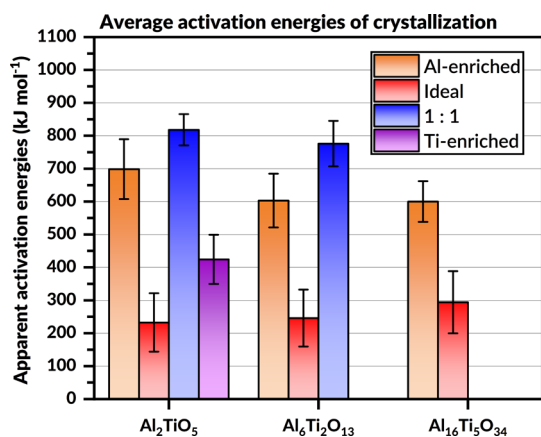


Figure 7. Bar diagrams showing the averaged apparent activation energies for various Al–Ti ratios and the phases  $\text{Al}_2\text{TiO}_5$ ,  $\text{Al}_6\text{Ti}_2\text{O}_{13}$ , and  $\text{Al}_{16}\text{Ti}_5\text{O}_{34}$ .

incorporate any elastic strains found among thin films and coatings.<sup>77</sup>

In eq 8,  $\Delta G_v$  is negative<sup>81–83</sup> due to the favorable exothermic nature of crystallization, whereas both  $\Delta G_s$  and  $\Delta G_e$  are typically positive,<sup>81–83</sup> thus acting unfavorably to nucleation's overall thermodynamic driving force. If the crystallization process is nucleation-controlled, then any factors influencing either  $\Delta G_n$  or  $\gamma$  will profoundly affect  $W^*$  and the general crystallization behavior. This will be expressed from variations in both activation energies and crystallization mechanisms with increasing temperature, especially at the earliest stages of crystallization. Such observations are noticed in Figures 4 and 6 and can also be seen in the T–T–T diagrams in Figure 5.

Second, the chemical composition may also strongly affect the crystallization process if it is nucleation-controlled.<sup>1,2,20</sup>

This is illustrated by the various kinetic parameters and  $E_a^{\text{app}}$  values depending on the amorphous samples' Al–Ti ratio. To understand this behavior and provide a conceptual explanation of the effect of supersaturation, we recall that

$$\Delta G_n = \Delta H_{\text{cryst}} - T\Delta S_{\text{cryst}} \quad (9)$$

where  $\Delta H_{\text{cryst}}$  denotes the total enthalpy of crystallization and  $\Delta S_{\text{cryst}}$  the change in entropy between the amorphous and crystalline states. As we explain in the following paragraphs, when nucleation governs the overall crystallization process, the entropy term will become the dominating term influencing the thermodynamic driving force of nucleation.

Formally, entropy can be defined from the Boltzmann–Planck equation, which treats entropy  $S$  as the sum of the available microstates  $\Omega$  with a certain probability of being occupied  $p$  as

$$S = -k_B \sum_i^\Phi p_i \ln \Omega_i \quad (10)$$

where  $\Phi$  marks the maximum possible configurations in the system. For nucleation to occur, a cooperative set of configurations in the amorphous state must start to match those found in the crystalline one,<sup>71</sup> thereby creating an ordered cluster of elements comprising the nucleus.<sup>2,15,74</sup> In this regard, two main contributions to  $S$  can be found in crystallization:<sup>84</sup> vibrational entropy ( $S_{\text{vib}}$ ), representing the vibrations atoms may undergo due to any temperature changes, and configurational entropy ( $S_{\text{config}}$ ), representing the discrete number of places where the atoms can be spatially positioned.<sup>84,85</sup> Because  $S_{\text{vib}}$  is frequently positive and tends to increase with temperature,<sup>84,86</sup> we can presume that  $\partial S_{\text{vib}}/\partial T > 0$ , so that the term beneficially affects nucleation's overall thermodynamic driving force, especially at increasing temperatures. Thus, this leaves us to focus on the change in



configurational entropy during crystallization,  $\Delta S_{\text{config}}$ , which marks the difference in possible configurations between the crystalline and amorphous states.<sup>81,87</sup> Unlike  $S_{\text{vib}}$ , the change in configurational entropy must always be a negative value because the total entropy of the amorphous state can never be less than that of the crystalline one (which inevitably would lead to the so-called Kauzmann's paradox).<sup>71</sup> Accordingly, for a nucleation-controlled process,  $\Delta S_{\text{config}}$  represents a significant contributor to any excess entropy found in the amorphous system.<sup>84</sup> Typically, large values of  $\Delta S_{\text{config}}$  signify that substantial differences between the amorphous and crystalline states exist,<sup>71,81</sup> meaning that extensive structural rearrangements—like bond redistributions and diffusion—are required to initialize any nucleation events. In contrast, small values of  $\Delta S_{\text{config}}$  demonstrate that considerable structural resemblances instead exist between the amorphous and crystalline states,<sup>71</sup> hence favoring the thermodynamic driving force of nucleation. Knowing that the number of configurations represented in  $S$  relates to the chemical potential  $\mu_i$  of the system according to the following expression<sup>88</sup>

$$\mu_i \equiv -T \left( \frac{\partial S}{\partial N_i} \right)_{U,V} \quad (11)$$

it becomes feasible, in theory, to modify the entropy term by varying the composition, which is represented by the number of particles  $N_i$  in eq 11. Consequently, for a nucleation-controlled crystallization process,  $\Delta S_{\text{config}}$  designates a fundamental parameter determining the overall driving force of nucleation, implying that  $W^*$  can be tailored by altering the chemical composition of the amorphous matrixes. In turn, this opens up new routes to achieve phase selectivity by nucleation<sup>2,79,89</sup> because the phase(s) most likely to be formed are those having the lowest values of their  $W^*$  and not necessarily those being the most thermodynamically stable ones.<sup>1,5,90</sup>

To emphasize the role of configurational entropy, we invoke from our previous studies that a short-range order of  $\text{Al}_2\text{TiO}_5$ ,  $\text{Al}_6\text{Ti}_2\text{O}_{13}$ , and  $\text{Al}_{16}\text{Ti}_5\text{O}_{34}$  exists in the amorphous samples.<sup>31</sup> Moreover, all of these phases display cationic mixing in their crystalline states, meaning that their cations can interchangeably reside in the available interstices.<sup>33,38,42,45,91,92</sup> Supported by the elemental homogeneity of the samples<sup>31</sup> and in light of previous reasonings, we can thus deduce that substantial structural similarities exist between the amorphous and crystalline states. Hence, low  $\Delta S_{\text{config}}$  values are expected for  $\text{Al}_2\text{TiO}_5$  and its co-forming  $\text{Al}_6\text{Ti}_2\text{O}_{13}$  and  $\text{Al}_{16}\text{Ti}_5\text{O}_{34}$  phases during their crystallization. In terms of crystallizing the main  $\text{Al}_2\text{TiO}_5$  phase, the lowest possible value of  $\Delta S_{\text{config}}$  is given when the stoichiometry of the amorphous matrix is nearest to the ideal one. For this particular case,  $S_{\text{config}}^{\text{crystal}}$  and  $S_{\text{config}}^{\text{amorph}}$  become the most alike, so that their corresponding  $\Delta S_{\text{config}}$  becomes closest to—although not equal to—zero. Essentially, this extremum represents a theoretical maximum in thermodynamic driving force of nucleation because most of the residual  $\Delta S_{\text{config}}$  then diminishes and  $\Delta G_n$  becomes predominantly governed by the enthalpy term ( $\Delta H_{\text{cryst}}$ ), as per eq 9. Noticeably, because  $\Delta H_{\text{cryst}}$  relates with the energies associated with breaking and redistributing chemical bonds during nucleation,<sup>5,71</sup> this condition implies that only minor readjustments of the local short range should be needed to initialize, and potentially finalize, the overall crystallization process.<sup>2</sup> Presumably, such readjustments would mainly involve changes

in oxygen's bonding characteristics because a short-range order of Al–O–Ti bonds already exists<sup>31</sup> and there is no apparent preference in either titanium's or aluminum's site preferences. Accordingly, by noting the aforementioned entropic condition and assuming that the crystal amorphous surface energy  $\gamma$  remains reasonably unaffected by temperature,<sup>76,78,82</sup> we can deduce using eq 7 that the lowest barrier of nucleation  $W^*$  is reached when the stoichiometry is closest to the ideal case. Indeed, this agrees well with our results in Figures 6 and 7, where the lowest  $E_a^{\text{app}}$  values are observed for the  $\sim$ ideal stoichiometry.

Interestingly, similar reasoning makes it also possible to predict when the lowest thermodynamic force of nucleation is obtained, resulting in the highest nucleation barrier. As seen in Figure 6, the highest initial  $E_a^{\text{app}}$  values are obtained when the Al–Ti ratio is equimolar (1:1). Structurally, this stoichiometry represents the closest scenario when there is no permutational preference in the placement of the individual cations, that is, all available interstices for the cations are treated as symmetrically equivalent.<sup>85</sup> For this case, the maximum randomness in possible configurations<sup>85,93,94</sup> is achieved so that the configurational entropy of the amorphous state reaches its uppermost value. Accordingly,  $\Delta S_{\text{config}}$  converts into its most positive value in eq 9, yielding the lowest net thermodynamic driving force of nucleation. In turn, this leads to a corresponding increase of the nucleation barrier  $W^*$ , as per eq 7.

Although it is argued that  $\Delta S_{\text{config}}$  has a crucial role in determining nucleation's overall thermodynamic driving force, particularly if the crystallization process is nucleation-controlled, it cannot entirely describe its link to the chemical composition. If that were the case, the  $\sim$ ideal composition would have been the sole stoichiometry displaying the lowest barrier of nucleation, which is not reflected in our results. Instead, the lowest values of  $W^*$  are shared between the  $\sim$ ideal and the Ti-enriched samples, whose initial  $E_a^{\text{app}}$  values are strikingly similar to each other. Essentially, this implies that these stoichiometries can have a joint nucleation behavior. Besides the similarities between these compositions'  $E_a^{\text{app}}$  values at the beginning of crystallization, the shared nucleation behavior is also reflected from their similar kinetics, particularly at the lowest annealing temperatures. Furthermore, while  $\Delta S_{\text{config}}$  incorporates the total effect of composition in the thermodynamic driving force by any excess in chemical potential, the term cannot unambiguously separate the individual contributions from the elements involved during crystallization. Therefore, it becomes clear that the apparent link in  $E_a^{\text{app}}$  values and shared kinetic behaviors between the  $\sim$ ideal and Ti-enriched stoichiometries can only be explained by solely considering one element's effect on the nucleation, namely, the role of titanium.

First, the Ti-enriched samples consistently demonstrated the lowest annealing temperatures to initiate any crystallization, implying the lowest value on  $W^*$  when the titanium content increases. Second, the calculated  $E_a^{\text{app}}$  values vary significantly depending on the Al–Ti ratio, and the derived values are consistently lower in the Ti-enriched regime than in the Al-enriched one. Third, in terms of their kinetic parameters, the  $\sim$ ideal and Ti-enriched stoichiometries displayed the largest dimensionalities ( $n$ ) on their crystallization, particularly at the lowest annealing temperatures. These values, being above four,<sup>83</sup> signify a transient nucleation behavior<sup>70</sup> where crystallization progresses from very small nuclei,<sup>65</sup> that is, the critical radius  $r^*$  becomes negligible as the total driving force

for nucleation increases immensely.<sup>30,59</sup> All things considered, we can thus conclude that titanium, as an element, plays an essential part in any nucleation events, especially for the main  $\text{Al}_2\text{TiO}_5$  phase.

**Secondary Nucleation and the Role of Diffusion.** If the overall crystallization is governed by nucleation, what influence does diffusion have? Although “nucleation control” does not necessarily imply “diffusion less”,<sup>74</sup> several factors speak about its diminished role during crystallization, especially for the  $\sim$ ideal stoichiometric case. Markedly, for a homogenous amorphous composition being close to a stoichiometric phase, where a short-range order exists along with few crystallographic constraints on the individual placements of cations, the requirements for diffusion during crystallization should, in theory, become minimal. However, when the stoichiometry of the amorphous matrix starts becoming non-stoichiometric and deviates from the emerging nuclei, the effect of diffusion should increasingly become more pronounced,<sup>30</sup> particularly in the short-to-medium range. Such compositional discrepancies can create peculiar transition features due to competing or synergetic interactions between nucleation and growth.<sup>20,74,78,79</sup> Noticeably, such behaviors are observed in the Al-enriched regime where a continuous crystallization of  $\text{Al}_{16}\text{Ti}_5\text{O}_{34}$  happens at the 660 °C annealing temperature. In most crystallizations, termination effects ensue at the later transition stages due to an exhaustion of the amorphous matrix and increasing impingements between the domain boundaries of the formed nuclei,<sup>66,95</sup> thus yielding the typical sigmoidal-shaped transformation curves. Consequently, the lack of such appearance in the aforementioned situation shows that these termination effects are either being absent or, more likely, lagging. In our case, this permits crystallization to proceed through new mechanisms that are fundamentally linked to—albeit considerably different—the previous ones.

These mechanisms include secondary nucleation, which arises due to energetically favorable interactions between pregrown parent crystals and the amorphous matrix.<sup>96</sup> Specifically, secondary nucleation is favored under conditions of high supersaturations and limited diffusion, where the presence of parent crystals enables nucleation to proceed heterogeneously with reduced energies and lower saturation levels than the original primary process does.<sup>96</sup> Strikingly, these conditions are reached in the Al-enriched regime during annealing at intermediate temperatures. Therefore, in this section, we describe the origin of the continuous crystallization behavior to several possible and concurrent nucleation mechanisms during crystallization. In particular, structural relaxations—which we have shown to exist with Raman spectroscopy<sup>31</sup>—may induce secondary nucleation events where new, structurally related phases, like  $\text{Al}_6\text{Ti}_2\text{O}_{13}$  and  $\text{Al}_{16}\text{Ti}_5\text{O}_{34}$ , are preferentially nucleated by slight readjustments of the cationic coordination. The largest  $\text{Al}_{16}\text{Ti}_5\text{O}_{34}$  phase may then grow through interactions between pregrown  $\text{Al}_2\text{TiO}_5$  grains and any heterogeneously emerging  $\text{Al}_6\text{Ti}_2\text{O}_{13}$  nuclei. This process, accentuated by the features seen in Figure 3, resembles that of Ostwald ripening, which we also explicate in this section.

As expressed in the previous section, titanium is likely to have an essential role in nucleating the main  $\text{Al}_2\text{TiO}_5$  phase. Therefore, when the stoichiometry of the amorphous matrix is Al-enriched, the deficiency of titanium will slowly deplete the element as it becomes incorporated into any emerging crystals by the process of primary nucleation. Likewise, the excess of

aluminum will then start to accumulate in the surrounding, untransformed amorphous matrix, especially within the short-to-intermediate range. As a result, the crystals' growth will gradually become impeded due to increasing steric constraints and the requirements of progressively longer diffusion distances. As seen in Figure 1 and the Al-enriched 660 °C transformation, this process seemingly culminates after about 40% of the volume fraction has finished. Mechanistically, the hampering of diffusion in amorphous solids relates to an increased viscosity of the matrix,<sup>20,61,72,78</sup> which can be expressed from the Stokes–Einstein relation<sup>97</sup>

$$D = \frac{k_B T}{6\pi\lambda\eta} \quad (12)$$

where  $D$  is an effective diffusion constant,  $\lambda$  is the radius of the diffusing element, and  $\eta$  is the viscosity. Although the above expression is derived for amorphous bulk materials,<sup>87</sup> it is regularly assumed that the viscosity behavior is similar among thin films and coatings.<sup>76,98</sup>

At intermediate annealing temperatures, where the untransformed amorphous state is left in an exorbitant energetic state (and the diffusion barrier is likewise), it becomes increasingly more viable for the transformation to continue through other possible, less-energy demanding routes. Such routes include, for instance, viscosity-driven structural relaxations. Generally, it is well-known that amorphous materials can relieve some of their excess energies through such relaxations,<sup>71,79,81,99,100</sup> wherein bond angles and distances are shifted and altered to adapt to new and exposed energy landscapes. The presence of structural relaxations within our amorphous samples can be linked to our previous Raman spectroscopic evaluations, showing that extensive structural rearrangements and coordination changes occur during annealing.<sup>31</sup> In addition, because there are few constraints on the individual placements of cations in  $\text{Al}_2\text{TiO}_5$ , owing to cationic mixing,<sup>33,42,91,92</sup> these reorganizations may also induce secondary nucleation events where structurally related phases are formed besides the main  $\text{Al}_2\text{TiO}_5$  phase. Such phases include  $\text{Al}_6\text{Ti}_2\text{O}_{13}$  and  $\text{Al}_{16}\text{Ti}_5\text{O}_{34}$ , whose crystallographic differences compared to  $\text{Al}_2\text{TiO}_5$  are very subtle, and can primarily be traced to different stacking sequences along the phases' respective  $c$ -axes, leading to elongations of ditto.<sup>38,41,44,45</sup> In turn, these elongations are caused by lower coordinating domains, especially for  $\text{Al}_6\text{Ti}_2\text{O}_{13}$  and  $\text{Al}_{16}\text{Ti}_5\text{O}_{34}$ .<sup>38,41</sup> Thus, any structural reorganization where the bond angles and distances are shifted would likely suffice to crystallize either one of these three phases, that is, either by the process of primary nucleation or that of possible secondary nucleation.

However, secondary nucleation does not wholly explain the continuous development of the  $\text{Al}_{16}\text{Ti}_5\text{O}_{34}$  phase in the Al-enriched domain, suggesting that an additional component is entangled in this phase's formation. Principally, this idea is supported by the observations made in Figure 3, where the  $\text{Al}_{16}\text{Ti}_5\text{O}_{34}$  phase progressively becomes larger while  $\text{Al}_6\text{Ti}_2\text{O}_{13}$  simultaneously diminishes. Given the occurrence of secondary nucleation, this observation can then be explained by the process of Ostwald ripening. This phenomenon has previously been invoked to explain comparable transition features in the synthesis of barium titanates,<sup>101</sup> zeolites,<sup>102</sup> and metal-selenide thin films.<sup>16</sup> For our particular case, Ostwald ripening explains how small nuclei of  $\text{Al}_6\text{Ti}_2\text{O}_{13}$ —formed by possibilities of

secondary nucleation—may dissolve and become incorporated into surrounding, pre-existing grains of  $\text{Al}_2\text{TiO}_5$ , allowing continuous growth and formation of the  $\text{Al}_{16}\text{Ti}_5\text{O}_{34}$  phase. Markedly, this explanation complies with the structural descriptions of  $\text{Al}_{16}\text{Ti}_5\text{O}_{34}$ , which are given as a combined (intergrowth) phase between  $\text{Al}_2\text{TiO}_5$  and  $\text{Al}_6\text{Ti}_2\text{O}_{13}$ .<sup>38</sup> Accordingly, we can apply two possible mechanisms to describe the formation of  $\text{Al}_{16}\text{Ti}_5\text{O}_{34}$ . One, where the phase nucleates directly in the amorphous matrix by primary nucleation and two, where the phase forms through interactions between  $\text{Al}_2\text{TiO}_5$  and  $\text{Al}_6\text{Ti}_2\text{O}_{13}$  by secondary nucleation and subsequent Ostwald ripening. Both of these processes are schematically explained in Figure 8.

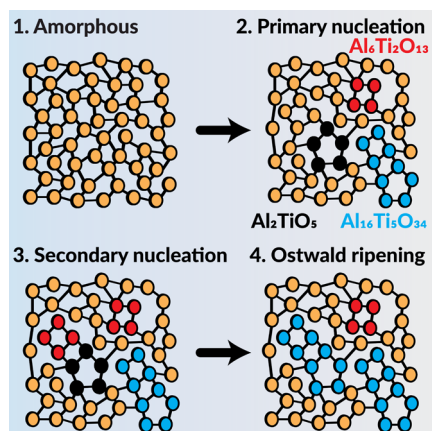


**Figure 8.** Schematic description of the multiple nucleation pathways to form  $\text{Al}_2\text{TiO}_5$  (black),  $\text{Al}_6\text{Ti}_2\text{O}_{13}$  (red), and  $\text{Al}_{16}\text{Ti}_5\text{O}_{34}$  (blue) during crystallization.

Because secondary nucleation can be initiated by only slight readjustments in bond angles and distances, it will not require any exaggerated diffusion to occur; thus, it can happen even in situations where diffusion is significantly impeded or reduced. For this reason, we expect the mechanisms controlling this feature to happen not only very locally but also very rapidly because structural relaxations should be a much faster process than any potential diffusion.<sup>71</sup> Interestingly, this is supported by the derived kinetic parameters found in Figure 4 describing this process (second regime), where the fastest crystallization rate ( $\ln K$ ) and most constrained ( $n$ ) nucleation behavior is observed. Typically, low values of  $n$  indicate that the crystallization is surface-mediated,<sup>63</sup> which is expected for secondary nucleation and agrees with observations made in other studies.<sup>1,16,67,96</sup> Also, the derived kinetic values of the second regime are highly deviant from the rest in the Al-enriched domain, emphasizing that they must represent a separate kinetic process during the crystallization.

Nonetheless, as explained in the method section, the kinetic parameters cannot entirely separate nucleation from growth because these processes are highly intertwined and intrinsic to the  $\ln K$  parameter.<sup>56</sup> For that reason, even if we have illustrated that nucleation is thermodynamically advantaged, it remains challenging to determine the extent of any diffusion involved in the continuous crystallization of the  $\text{Al}_{16}\text{Ti}_5\text{O}_{34}$  phase. This particularly concerns the process of Ostwald ripening because it seemingly happens during intermediate-to-late transition stages.

Irrespectively, the findings from this study provide a conceptual understanding of why the  $\text{Al}_6\text{Ti}_2\text{O}_{13}$  and  $\text{Al}_{16}\text{Ti}_5\text{O}_{34}$  phases have not been commonly observed using conventional solid-state synthesis methods. Crystallization from amorphous intermediates—compared to solid-state methods—may readily operate in two different kinetic regimes. Although the former can be nucleation-controlled, the latter techniques essentially remain diffusion-controlled. In this respect, it is interesting to note that Hoffmann *et al.* used non-equilibrium conditions such as rapid heating and quenching when first synthesizing  $\text{Al}_{16}\text{Ti}_5\text{O}_{34}$  by the solid-state route.<sup>38</sup> Accordingly, combined with the findings of this study, this tells us that nucleation—rather than diffusion—should be the key mechanism to control the formation of  $\text{Al}_6\text{Ti}_2\text{O}_{13}$  and  $\text{Al}_{16}\text{Ti}_5\text{O}_{34}$ , particularly by the crystallization of amorphous intermediates.

## CONCLUSIONS

A multivariate kinetic study has been made to elucidate the effect of the composition (Al–Ti ratio) and isothermal annealing temperature when crystallizing amorphous  $\text{Al}_2\text{TiO}_5$ -based coatings. The combined results reveal a strong temperature dependency on the transformations, particularly at the earliest transition stages where nucleation is the main governing process. The co-crystallization of structurally related phases to  $\text{Al}_2\text{TiO}_5$ , like  $\text{Al}_6\text{Ti}_2\text{O}_{13}$  and  $\text{Al}_{16}\text{Ti}_5\text{O}_{34}$ , readily occurs when the composition is Al-enriched or  $\sim$ ideal but not when the composition reaches into the equimolar or Ti-enriched domains where anatase starts to appear instead. The Al-enriched samples demonstrated the strongest reluctance to transform and the largest thermal stability of its amorphous phase. Moreover, peculiar transition behaviors were noticed in this compositional domain when intermediate annealing temperatures (660 °C) were used. A shift into a continuous, linear transformation regime occurred for the  $\text{Al}_{16}\text{Ti}_5\text{O}_{34}$  phase, which did not terminate even after prolonged annealing durations. This behavior is ascribed to several possible nucleation mechanisms during the crystallization, including secondary nucleation caused by structural relaxations of the amorphous matrixes. In turn, the interactions between emerging  $\text{Al}_6\text{Ti}_2\text{O}_{13}$  nuclei and pre-existing  $\text{Al}_2\text{TiO}_5$  grains can lead to the continuous growth of the  $\text{Al}_{16}\text{Ti}_5\text{O}_{34}$  phase through Ostwald ripening.

Detailed insights into the crystallization process were obtained from kinetic analyses using the JMAK equation. A reverse relationship between the overall crystallization rate (expressed from  $\ln K$ ) and the dimensionality of the crystallization (described from the parameter  $n$ ) was revealed. This implies that a more heterogeneous transition character leads to faster transition rates. Moreover, the  $\sim$ ideal and Ti-enriched sample compositions displayed the largest dimensionalities on their crystallization and transient nucleation behaviors, suggesting that nucleation is highly favored and occurs homogeneously in the amorphous matrixes. By linking the displayed results between the  $\sim$ ideal stoichiometry and the Ti-enriched, we show that titanium is crucial in nucleating the  $\text{Al}_2\text{TiO}_5$  phase. Combined with the apparent activation energies for crystallization, where the  $\sim$ ideal and Ti-enriched cases exhibited the lowest values, we also show that the overall amorphous-to-crystalline transition is nucleation-controlled. In this specific kinetic regime, the role of the configurational entropy becomes essential as it governs most of the thermodynamic driving force of crystallization.



The configurational entropy of  $\text{Al}_2\text{TiO}_5$  has previously been attributed to be responsible for the phase's entropy stabilization at higher temperatures. Herein, we also demonstrate that it plays a central part in the nucleation behavior from the amorphous state. This finding may open up novel synthesis routes to make oxide compounds in general and achieve better phase selectivity in particular.

## ■ ASSOCIATED CONTENT

### SI Supporting Information

The Supporting Information is available free of charge at <https://pubs.acs.org/doi/10.1021/acs.chemmater.2c00615>.

**Content:** EDS and Rutherford backscattering, relative phase fraction data, derivations of kinetic parameters, apparent activation energies, and phase formation analyses. (PDF)

## ■ AUTHOR INFORMATION

### Corresponding Author

**Mats Boman** – Department of Chemistry, Inorganic Chemistry, Ångström Laboratory, Uppsala University, Uppsala SE-75121, Sweden; Email: [Mats.Boman@kemi.uu.se](mailto:Mats.Boman@kemi.uu.se)

### Authors

**Sebastian Öhman** – Department of Chemistry, Inorganic Chemistry, Ångström Laboratory, Uppsala University, Uppsala SE-75121, Sweden; [orcid.org/0000-0002-7071-3917](https://orcid.org/0000-0002-7071-3917)

**Gustav Ek** – Department of Chemistry, Inorganic Chemistry, Ångström Laboratory, Uppsala University, Uppsala SE-75121, Sweden; [orcid.org/0000-0003-4831-3842](https://orcid.org/0000-0003-4831-3842)

**Gyula Nagy** – Department of Physics and Astronomy, Applied Nuclear Physics, Ångström Laboratory, Uppsala University, Uppsala SE-75120, Sweden; [orcid.org/0000-0003-3172-5736](https://orcid.org/0000-0003-3172-5736)

**Tobias Törndahl** – Department of Materials Science and Engineering, Solar Cell Technology, Ångström Laboratory, Uppsala University, Uppsala SE-75103, Sweden; [orcid.org/0000-0001-7757-5847](https://orcid.org/0000-0001-7757-5847)

**Daniel Primetzhofer** – Department of Physics and Astronomy, Applied Nuclear Physics, Ångström Laboratory, Uppsala University, Uppsala SE-75120, Sweden; [orcid.org/0000-0002-5815-3742](https://orcid.org/0000-0002-5815-3742)

Complete contact information is available at:

<https://pubs.acs.org/doi/10.1021/acs.chemmater.2c00615>

### Author Contributions

S.Ö.—conceptualization, syntheses, formal analyses XRD and EDS, visualization, and writing—original draft except for RBS measurements. G.E.—data extraction, peak modeling, and XRD refinements. G.N.—RBS and ion beam spectroscopic measurements. T.T.—supervision, review, and editing. D.P.—Director of Tandem laboratory, funding acquisition and supervision and guidance of RBS and ion beam spectroscopic measurements. M.B.—funding acquisition, project administration, and supervision.

### Notes

The authors declare no competing financial interest.

## ■ ACKNOWLEDGMENTS

The Swedish Foundation for Strategic Research (SSF), contract RMA15-0048, is acknowledged for its financial support. Furthermore, support from VR-RFI (#2017-00646\_9) and SSF (#2019-00191) for accelerator operation at Uppsala University is also gratefully acknowledged. The authors would like to thank Mikael Ottosson, Department of Chemistry—Uppsala University, for technical support of the diffractometers used in this study.

## ■ REFERENCES

- (1) Noh, M.; Johnson, C. D.; Hornbostel, M. D.; Thiel, J.; Johnson, D. C. Control of Reaction Pathway and the Nanostructure of Final Products through the Design of Modulated Elemental Reactants. *Chem. Mater.* **1996**, *8*, 1625–1635.
- (2) Oyelaran, O.; Novet, T.; Johnson, C. D.; Johnson, D. C. Controlling Solid-State Reaction Pathways: Composition Dependence in the Nucleation Energy of InSe. *J. Am. Chem. Soc.* **1996**, *118*, 2422–2426.
- (3) Martinolich, A. J.; Kurzman, J. A.; Neilson, J. R. Circumventing Diffusion in Kinetically Controlled Solid-State Metathesis Reactions. *J. Am. Chem. Soc.* **2016**, *138*, 11031–11037.
- (4) Barboux, P.; Griesmar, P.; Ribot, F.; Mazerolles, L. Homogeneity-Related Problems in Solution Derived Powders. *J. Solid State Chem.* **1995**, *117*, 343–350.
- (5) Novet, T.; Johnson, D. C. New Synthetic Approach to Extended Solids: Selective Synthesis of Iron Silicides via the Amorphous State. *J. Am. Chem. Soc.* **1991**, *113*, 3398–3403.
- (6) Fister, L.; Johnson, D. C.; Brown, R. Synthesis of copper-molybdenum-selenium ( $\text{Cu}_x\text{Mo}_6\text{Se}_8$ ) without binary compounds as intermediates: a study using superlattices to kinetically control a solid-state reaction. *J. Am. Chem. Soc.* **1994**, *116*, 629–633.
- (7) Jansen, M. A Concept for Synthesis Planning in Solid-State Chemistry. *Angew. Chem., Int. Ed.* **2002**, *41*, 3746–3766.
- (8) Ilatovskaia, M.; Savinykh, G.; Fabrichnaya, O. Thermodynamic Description of the Ti–Al–O System Based on Experimental Data. *J. Phase Equilib. Diffus.* **2017**, *38*, 175–184.
- (9) Stein, A.; Keller, S. W.; Mallouk, T. E. Turning down the Heat: Design and Mechanism in Solid-State Synthesis. *Science* **1993**, *259*, 1558–1564.
- (10) Gopalakrishnan, J.; Bhuvanesh, N. S.; Rangan, K. K. Towards Rational Synthesis of Inorganic Solids. *Curr. Opin. Solid State Mater. Sci.* **1996**, *1*, 285–294.
- (11) Aykol, M.; Montoya, J. H.; Hummelshøj, J. Rational Solid-State Synthesis Routes for Inorganic Materials. *J. Am. Chem. Soc.* **2021**, *143*, 9244–9259.
- (12) Martinolich, A. J.; Neilson, J. R. Toward Reaction-by-Design: Achieving Kinetic Control of Solid State Chemistry with Metathesis. *Chem. Mater.* **2017**, *29*, 479–489.
- (13) Sun, W.; Dacek, S. T.; Ong, S. P.; Hautier, G.; Jain, A.; Richards, W. D.; Gamst, A. C.; Persson, K. A.; Ceder, G. The Thermodynamic Scale of Inorganic Crystalline Metastability. *Sci. Adv.* **2016**, *2*, No. e1600225.
- (14) Justl, A. P.; Cerretti, G.; Bux, S. K.; Kauzlarich, S. M.  $2 + 2 = 3$ : Making Ternary Phases through a Binary Approach. *Chem. Mater.* **2022**, *34*, 1342–1355.
- (15) Fister, L.; Johnson, D. C. Controlling Solid-State Reaction Mechanisms Using Diffusion Length in Ultrathin-Film Superlattice Composites. *J. Am. Chem. Soc.* **1992**, *114*, 4639–4644.
- (16) Noh, M.; Thiel, J.; Johnson, D. C. Synthesis of Crystalline Superlattices by Controlled Crystallization of Modulated Reactants. *Science* **1995**, *270*, 1181–1184.
- (17) Sutter-Fella, C. M. The Value of Watching How Materials Grow: A Multimodal Case Study on Halide Perovskites. *Adv. Energy Mater.* **2021**, *11*, 2003534.



- (18) Martinolich, A. J.; Kurzman, J. A.; Neilson, J. R. Polymorph Selectivity of Superconducting CuSe<sub>2</sub> through Kinetic Control of Solid-State Metathesis. *J. Am. Chem. Soc.* **2015**, *137*, 3827–3833.
- (19) Vioux, A. Nonhydrolytic Sol–Gel Routes to Oxides. *Chem. Mater.* **1997**, *9*, 2292–2299.
- (20) Perepezko, J. H. Nucleation-Controlled Reactions and Metastable Structures. *Prog. Mater. Sci.* **2004**, *49*, 263–284.
- (21) Ziegler, J. F.; Mayer, J. W.; Kircher, C. J.; Tu, K. N. Kinetics of the Formation of Hafnium Silicides on Silicon. *J. Appl. Phys.* **1973**, *44*, 3851–3857.
- (22) Rosenblum, M. P.; Turnbull, D. Bias Sputter Deposition of Pd–Au–Si and Pd–Si: Composition and Thermal Behavior. *J. Non-Cryst. Solids* **1980**, *37*, 45–51.
- (23) Majni, G.; Costato, M.; Panini, F. The Growth Processes of Thin Film Silicides in Si/Ni Planar Systems. *Thin Solid Films* **1985**, *125*, 71–78.
- (24) Herd, S.; Tu, K. N.; Ahn, K. Y. Formation of an amorphous Rh–Si alloy by interfacial reaction between amorphous Si and crystalline Rh thin films. *Appl. Phys. Lett.* **1983**, *42*, 597–599.
- (25) Canali, C.; Majni, G.; Ottaviani, G.; Celotti, G. Phase diagrams and metal-rich silicide formation. *J. Appl. Phys.* **1979**, *50*, 255–258.
- (26) Nava, F.; Psaras, P. A.; Takai, H.; Tu, K. N. Phase Transformations in Alloy and Bilayer Thin Films of Vanadium and Silicon. *J. Appl. Phys.* **1986**, *59*, 2429–2438.
- (27) Gas, P.; d’Heurle, F. M.; LeGoues, F. K.; La Placa, S. J. Formation of intermediate phases, Ni<sub>3</sub>Si<sub>2</sub> and Pt<sub>6</sub>Si<sub>5</sub>: Nucleation, identification, and resistivity. *J. Appl. Phys.* **1986**, *59*, 3458–3466.
- (28) Gas, P.; Tardy, F. J.; d’Heurle, F. M. Disilicide solid solutions, phase diagram, and resistivities. I. TiSi<sub>2</sub>–WSi<sub>2</sub>. *J. Appl. Phys.* **1986**, *60*, 193–200.
- (29) Coulman, B.; Chen, H. Kinetics of Pd<sub>2</sub>Si layer growth measured by an x-ray diffraction technique. *J. Appl. Phys.* **1986**, *59*, 3467–3474.
- (30) Lange, F. F.; Balmer, M. L.; Levi, C. G. Diffusion limited crystallization and phase partitioning in ZrO<sub>2</sub>–metal oxide binary systems. *J. Sol-Gel Sci. Technol.* **1994**, *2*, 317–321.
- (31) Öhman, S.; Qiu, R.; Edvinsson, T.; Bäcke, O.; Törndahl, T.; Boman, M. Selective Kinetic Growth and Role of Local Coordination in Forming Al<sub>2</sub>TiO<sub>5</sub>-Based Coatings at Lower Temperatures. *Mater. Adv.* **2021**, *2*, 5737–5751.
- (32) Low, I. M.; Skala, R. D.; Zhou, D. Synthesis of Functionally Gradient Aluminium Titanate/Alumina Composites. *J. Mater. Sci. Lett.* **1996**, *15*, 345–347.
- (33) Morosin, B.; Lynch, R. W. Structure studies on Al<sub>2</sub>TiO<sub>5</sub> at room temperature and at 600°C. *Acta Crystallogr., Sect. B: Struct. Sci., Cryst. Eng. Mater.* **1972**, *28*, 1040–1046.
- (34) Soofi, M.; Binz, L.; Anderson, M. W. Protective Coating Composition For Molten Aluminium and Alkali Metal Environments. U.S. Patent 10,233,335 B2, 2019.
- (35) Tian, S.; Sun, K.; Cui, H.; Xie, X.; Wang, X.; Wei, N.; Wang, H.; Wang, W.; Song, X.; Yang, K. Structural evolution and electrochemical corrosion behavior of Al–Ti–O amorphous-nano-crystalline composite films deposited by magnetron sputtering. *Thin Solid Films* **2019**, *692*, 137640.
- (36) Kim, H. C.; Lee, K. S.; Kweon, O. S.; Aneziris, C. G.; Kim, I. J. Crack Healing, Reopening and Thermal Expansion Behavior of Al<sub>2</sub>TiO<sub>5</sub> Ceramics at High Temperature. *J. Eur. Ceram. Soc.* **2007**, *27*, 1431–1434.
- (37) Low, I.-M.; Oo, Z. In Situ Diffraction Study of Self-Recovery in Aluminum Titanate. *J. Am. Ceram. Soc.* **2008**, *91*, 1027–1029.
- (38) Hoffmann, S.; Norberg, S. T.; Yoshimura, M. Structural models for intergrowth structures in the phase system Al<sub>2</sub>O<sub>3</sub>–TiO<sub>2</sub>. *J. Solid State Chem.* **2005**, *178*, 2897–2906.
- (39) Das, S. The Al–O–Ti (Aluminum–Oxygen–Titanium) System. *J. Phase Equilib.* **2002**, *23*, 525–536.
- (40) Bekker, T. B.; Litasov, K. D.; Shatskiy, A. F.; Sagatov, N. E.; Krinitsin, P. G.; Krashennnikov, S. P.; Podborodnikov, I. V.; Rashchenko, S. V.; Davydov, A. V.; Ohfujii, H. Towards the Investigation of Ternary Compound in the Ti–Al–Zr–O System: Effect of Oxygen Fugacity on Phase Formation. *J. Eur. Ceram. Soc.* **2020**, *40*, 3663–3672.
- (41) Hoffmann, S.; Norberg, S. T.; Yoshimura, M. Melt Synthesis of Al<sub>2</sub>TiO<sub>5</sub> Containing Composites and Reinvestigation of the Phase Diagram Al<sub>2</sub>O<sub>3</sub>–TiO<sub>2</sub> by Powder X-Ray Diffraction. *J. Electroceram.* **2006**, *16*, 327–330.
- (42) Skala, R. D.; Li, D.; Low, I. M. Diffraction, Structure and Phase Stability Studies on Aluminium Titanate. *J. Eur. Ceram. Soc.* **2009**, *29*, 67–75.
- (43) Kim, I. J.; Gauckler, L. G. Formation, Decomposition and Thermal Stability of Al<sub>2</sub>TiO<sub>5</sub> Ceramics. *J. Ceram. Sci. Technol.* **2012**, *3*, 49–60.
- (44) Norberg, S. T.; Ishizawa, N.; Hoffmann, S.; Yoshimura, M. Redetermination of  $\beta$ -Al<sub>2</sub>TiO<sub>5</sub> obtained by melt casting. *Acta Crystallogr., Sect. E: Crystallogr. Commun.* **2005**, *61*, i160–i162.
- (45) Norberg, S. T.; Hoffmann, S.; Yoshimura, M.; Ishizawa, N. Al<sub>6</sub>Ti<sub>2</sub>O<sub>13</sub>, a new phase in the Al<sub>2</sub>O<sub>3</sub>–TiO<sub>2</sub> system. *Acta Crystallogr., Sect. C: Struct. Chem.* **2005**, *61*, i35–i38.
- (46) Johnson, W. A.; Mehl, K. E. Reaction Kinetics in Processes of Nucleation and Growth. *Trans. Am. Inst. Min., Metall. Pet. Eng.* **1939**, *195*, 416–458.
- (47) Cantor, B. The Avrami Equation: Phase Transformations. In *The Equations of Materials*; Oxford University Press, 2020; pp 180–206.
- (48) Avrami, M. Kinetics of Phase Change. I General Theory. *J. Chem. Phys.* **1939**, *7*, 1103–1112.
- (49) Avrami, M. Kinetics of Phase Change. II Transformation-Time Relations for Random Distribution of Nuclei. *J. Chem. Phys.* **1940**, *8*, 212–224.
- (50) Avrami, M. Granulation, Phase Change, and Microstructure Kinetics of Phase Change. III. *J. Chem. Phys.* **1941**, *9*, 177–184.
- (51) Kolmogorov, A. N. Volume II: Probability Theory and Mathematical Statistics. In *Selected Works of A. N. Kolmogorov*; Shiryayev, A. N., Lindquist, G., Eds.; Springer International Publishing: Dordrecht, 1992; pp 188–192.
- (52) Coelho, A. A. TOPAS and TOPAS-Academic: an optimization program integrating computer algebra and crystallographic objects written in C++. *J. Appl. Crystallogr.* **2018**, *51*, 210–218.
- (53) Sarel, J.; Chen, H.; Jongste, J. F.; Radelaar, S. In Situ X-Ray Diffraction Study of the Formation of TiSi<sub>2</sub>–C<sub>49</sub> Phase from Ti–Si Multilayers on Si(100). *Mater. Chem. Phys.* **1995**, *40*, 82–86.
- (54) Zhuang, Y. X.; Jiang, J. Z.; Lin, Z. G.; Mezouar, M.; Crichton, W.; Inoue, A. Evidence of Eutectic Crystallization and Transient Nucleation in Al<sub>89</sub>La<sub>6</sub>Ni<sub>5</sub> Amorphous Alloy. *Appl. Phys. Lett.* **2001**, *79*, 743–745.
- (55) Liu, F.; Wang, H. F.; Chen, Z.; Yang, W.; Yang, G. C. Determination of Activation Energy for Crystallization in Amorphous Alloys. *Mater. Lett.* **2006**, *60*, 3916–3921.
- (56) Finney, E. E.; Finke, R. G. Is There a Minimal Chemical Mechanism Underlying Classical Avrami–Erofe’ev Treatments of Phase-Transformation Kinetic Data? *Chem. Mater.* **2009**, *21*, 4692–4705.
- (57) Mehta, N.; Kumar, A. Some New Observations on Activation Energy of Crystal Growth for Thermally Activated Crystallization. *J. Phys. Chem. B* **2016**, *120*, 1175–1182.
- (58) Lu, K.; Wang, J. T. Activation Energies for Crystal Nucleation and Growth in Amorphous Alloys. *Mater. Sci. Eng. A* **1991**, *133*, 500–503.
- (59) Buchwitz, M.; Adlwarth-Dieball, R.; Ryder, P. L. Kinetics of the Crystallization of Amorphous Ti<sub>2</sub>Ni. *Acta Metall. Mater.* **1993**, *41*, 1885–1892.
- (60) Ranganathan, S.; Von Heimendahl, M. The Three Activation Energies with Isothermal Transformations: Applications to Metallic Glasses. *J. Mater. Sci.* **1981**, *16*, 2401–2404.
- (61) Chen, Z.; Zhu, Q.; Li, Z.; Guo, Q.; Zhang, K.; Jiang, Y. Effects of Si/B Ratio on the Isothermal Crystallization Behavior of FeNiSiBCuNb Amorphous Alloys. *Thermochim. Acta* **2021**, *697*, 178854.

- (62) Mandal, S.; Lee, D.-E.; Park, T. Isothermal Crystallization Kinetics of (Cu<sub>60</sub>Zr<sub>25</sub>Ti<sub>15</sub>)<sub>99.3</sub>Nb<sub>0.7</sub> Bulk Metallic Glass. *Sci. Rep.* **2020**, *10*, 10577.
- (63) Lu, W.; Yan, B.; Huang, W.-h. Complex Primary Crystallization Kinetics of Amorphous Finemet Alloy. *J. Non-Cryst. Solids* **2005**, *351*, 3320–3324.
- (64) Blank-Bewersdorff, M.; Köster, U. Transient Nucleation in Zirconium-Based Metallic Glasses. *Mater. Sci. Eng.* **1988**, *97*, 313–316.
- (65) Sinha, I.; Mandal, R. K. Avrami Exponent under Transient and Heterogeneous Nucleation Transformation Conditions. *J. Non-Cryst. Solids* **2011**, *357*, 919–925.
- (66) Dill, E. D.; Josey, A. A.; Folmer, J. C. W.; Hou, F.; Martin, J. D. Experimental Determination of the Crystallization Phase-Boundary Velocity in the Halozeotype CZX-1. *Chem. Mater.* **2013**, *25*, 3932–3940.
- (67) Málek, J. Kinetic Analysis of Crystallization Processes in Amorphous Materials. *Thermochim. Acta* **2000**, *355*, 239–253.
- (68) Ye, F.; Lu, K. Crystallization Kinetics of Al-La-Ni Amorphous Alloy. *J. Non-Cryst. Solids* **2000**, *262*, 228–235.
- (69) Blázquez, J. S.; Conde, C. F.; Conde, A. Kinetics of nanocrystallization in FeCoNbB(Cu) alloys. *Appl. Phys. A: Mater. Sci. Process.* **2003**, *76*, S71–S75.
- (70) Vasiliev, S. V.; Tkatch, V. I.; Aronin, A. S.; Kovalenko, O. V.; Rassolov, S. G. Analysis of the Transient Behavior of Nucleation in the Fe<sub>40</sub>Ni<sub>40</sub>P<sub>14</sub>B<sub>6</sub> Glass. *J. Alloys Compd.* **2018**, *744*, 141–145.
- (71) Hou, F.; Martin, J. D.; Dill, E. D.; Folmer, J. C. W.; Josey, A. A. Transition Zone Theory of Crystal Growth and Viscosity. *Chem. Mater.* **2015**, *27*, 3526.
- (72) Vyazovkin, S. Activation Energies and Temperature Dependencies of the Rates of Crystallization and Melting of Polymers. *Polymers* **2020**, *12*, 1070.
- (73) Fernengel, W.; Kronmüller, H.; Rapp, M.; He, Y. The Activation Energy of Crystallization of Amorphous Fe<sub>40</sub>Ni<sub>40</sub>P<sub>14</sub>B<sub>6</sub>. *Appl. Phys. A: Solids Surf.* **1982**, *28*, 137–144.
- (74) Perepezko, J. H.; Uttormark, M. J. Nucleation-Controlled Solidification Kinetics. *Metall. Mater. Trans. A* **1996**, *27*, S33–S47.
- (75) Alexandrov, D. V.; Malygin, A. P. Transient Nucleation Kinetics of Crystal Growth at the Intermediate Stage of Bulk Phase Transitions. *J. Phys. A: Math. Theor.* **2013**, *46*, 455101.
- (76) Martinková, S.; Štěpánková, J.; Barták, J.; Málek, J. Transient Nucleation in Ge-Sb-S Thin Films. *Cryst. Growth Des.* **2018**, *18*, 4562–4570.
- (77) Abyzov, A. S.; Fokin, V. M.; Rodrigues, A. M.; Zanolto, E. D.; Schmelzer, J. W. P. The Effect of Elastic Stresses on the Thermodynamic Barrier for Crystal Nucleation. *J. Non-Cryst. Solids* **2016**, *432*, 325–333.
- (78) Thieme, K.; Avramov, I.; Rüssel, C. The Mechanism of Deceleration of Nucleation and Crystal Growth by the Small Addition of Transition Metals to Lithium Disilicate Glasses. *Sci. Rep.* **2016**, *6*, 25451.
- (79) Ge, X.; Hu, Q.; Lu, W.; Cao, S.; Yang, L.; Xu, M.; Xia, M.; Li, J. Polymorphic Transition and Nucleation Pathway of Barium Dtitanate (BaTi<sub>2</sub>O<sub>5</sub>) during Crystallization from Undercooled Liquid. *Sci. Rep.* **2019**, *9*, 7207.
- (80) Cantor, B. *The Equations of Materials*; Oxford University Press: Oxford, 2020.
- (81) Graeser, K. A.; Patterson, J. E.; Zeitler, J. A.; Rades, T. The Role of Configurational Entropy in Amorphous Systems. *Pharmaceutics* **2010**, *2*, 224–244.
- (82) Erdemir, D.; Lee, A. Y.; Myerson, A. S. Nucleation of Crystals from Solution: Classical and Two-Step Models. *Acc. Chem. Res.* **2009**, *42*, 621–629.
- (83) Kelton, K. F.; Greer, A. L.; Thompson, C. V. Transient Nucleation in Condensed Systems. *J. Chem. Phys.* **1983**, *79*, 6261–6276.
- (84) Smith, H. L.; Li, C. W.; Hoff, A.; Garrett, G. R.; Kim, D. S.; Yang, F. C.; Lucas, M. S.; Swan-Wood, T.; Lin, J. Y. Y.; Stone, M. B.; Abernathy, D. L.; Demetriou, M. D.; Fultz, B. Separating the Configurational and Vibrational Entropy Contributions in Metallic Glasses. *Nat. Phys.* **2017**, *13*, 900–905.
- (85) Kaußler, C.; Kieslich, G. CrystIT : Complexity and Configurational Entropy of Crystal Structures via Information Theory. *J. Appl. Crystallogr.* **2021**, *54*, 306–316.
- (86) Benisek, A.; Dachs, E. The Vibrational and Configurational Entropy of Disorder in Cu<sub>3</sub>Al. *J. Alloys Compd.* **2015**, *632*, S85–S90.
- (87) Zhou, D.; Zhang, G. G. Z.; Law, D.; Grant, D. J. W.; Schmitt, E. A. Thermodynamics, Molecular Mobility and Crystallization Kinetics of Amorphous Griseofulvin. *Mol. Pharm.* **2008**, *5*, 927–936.
- (88) Schroeder, D. V. Interactions and Implications. In *An Introduction to Thermal Physics*; Oxford University Press: Oxford, 2021; p 116.
- (89) Breu, J.; Seidl, W.; Huttner, D.; Kraus, F. Nucleation-Controlled Crystallization of a New, Spontaneously Resolved Solvate of [Ru(Bpy)<sub>3</sub>](PF<sub>6</sub>)<sub>2</sub> and Its Desolvation Reaction. *Chem.—Eur. J.* **2002**, *8*, 4454–4460.
- (90) Thompson, C. V.; Spaepen, F. Homogeneous Crystal Nucleation in Binary Metallic Melts. *Acta Metall.* **1983**, *31*, 2021–2027.
- (91) Ohya, Y.; Kawachi, Y.; Ban, T. Cation Distribution of Pseudobrookite-Type Titanates and Their Phase Stability. *J. Ceram. Soc. Jpn.* **2017**, *125*, 695–700.
- (92) Epicier, T.; Thomas, G.; Wohlfrohm, H.; Moya, J. S. High resolution electron microscopy study of the cationic disorder in Al<sub>2</sub>TiO<sub>5</sub>. *J. Mater. Res.* **1991**, *6*, 138–145.
- (93) Buschow, K. H. J. Crystallization of amorphous Zr<sub>1-x</sub>Cox alloys. *J. Less-Common Met.* **1982**, *85*, 221–231.
- (94) Xirouchakis, D. M. Pseudobrookite-Group Oxide Solutions and Basaltic Melts. *Lithos* **2007**, *95*, 1–9.
- (95) Martin, J. D. Particle Size Is a Primary Determinant for Sigmoidal Kinetics of Nanoparticle Formation: A “Disproof” of the Finke-Watzky (F-W) Nanoparticle Nucleation and Growth Mechanism. *Chem. Mater.* **2020**, *32*, 3651–3656.
- (96) Xu, S.; Hou, Z.; Chuai, X.; Wang, Y. Overview of Secondary Nucleation: From Fundamentals to Application. *Ind. Eng. Chem. Res.* **2020**, *59*, 18335–18356.
- (97) Lindqvist, C.; Sanz-Velasco, A.; Wang, E.; Bäcke, O.; Gustafsson, S.; Olsson, E.; Andersson, M. R.; Müller, C. Nucleation-Limited Fullerene Crystallisation in a Polymer-Fullerene Bulk-Heterojunction Blend. *J. Mater. Chem. A* **2013**, *1*, 7174–7180.
- (98) Stephens, R. B. The Viscosity and Structural Relaxation Rate of Evaporated Amorphous Selenium. *J. Appl. Phys.* **1978**, *49*, S855–S864.
- (99) Spinella, C.; Lombardo, S.; Priolo, F. Crystal Grain Nucleation in Amorphous Silicon. *J. Appl. Phys.* **1998**, *84*, S383–S414.
- (100) Mattern, N.; Eckert, J.; Seidel, M.; Kühn, U.; Doyle, S.; Bäcker, I. Relaxation and Crystallization of Amorphous Zr<sub>65</sub>Al<sub>7.5</sub>-Cu<sub>17.5</sub>Ni<sub>10</sub>. *Mater. Sci. Eng. A* **1997**, *226–228*, 468–473.
- (101) Zhan, H.; Yang, X.; Wang, C.; Chen, J.; Wen, Y.; Liang, C.; Greer, H. F.; Wu, M.; Zhou, W. Multiple Nucleation and Crystal Growth of Barium Titanate. *Cryst. Growth Des.* **2012**, *12*, 1247–1253.
- (102) Palčić, A.; Bronić, J.; Brlek, Đ.; Subotić, B. New Insights on the Autocatalytic Nucleation in Zeolite A Synthesis. *CrystEngComm* **2011**, *13*, 1215–1220.